Published in final edited form as:
Ann Biomed Eng. 2010 May ; 38(5): 1836–1853. doi:10.1007/s10439-010-9956-y.

Airway Wall Stiffening Increases Peak Wall Shear Stress: A Fluid-structure Interaction Study in Rigid and Compliant Airways

Guohua Xia[1,2], **Merryn H. Tawhai**[6], **Eric A. Hoffman**[3,4,5], and **Ching-Long Lin**[1,2,†]

[1] Department of Mechanical and Industrial Engineering, The University of Iowa, Iowa City, Iowa 52242 [2] Department of IIHR-Hydroscience & Engineering, The University of Iowa, Iowa City, Iowa 52242 [3] Department of Biomedical Engineering, The University of Iowa, Iowa City, Iowa 52242 [4] Department of Medicine, The University of Iowa, Iowa City, Iowa 52242 [5] Department of Radiology, The University of Iowa, Iowa City, Iowa 52242 [6] Bioengineering Institute, The University of Auckland, Auckland, New Zealand

Abstract

The airflow characteristics in a computed tomography (CT) based human airway bifurcation model with rigid and compliant walls are investigated numerically. An in-house three-dimensional (3D) fluid-structure interaction method is applied to simulate the flow at different Reynolds numbers and airway wall stiffness. As the Reynolds number increases, the airway wall deformation increases and the secondary flow becomes more prominent. It is found that the peak wall shear stress on the rigid airway wall can be five times stronger than that on the compliant airway wall. When adding tethering forces to the model, we find that these forces, which produce larger airway deformation than without tethering, lead to more skewed velocity profiles in the lower branches and further reduced wall shear stresses via a larger airway lumen. This implies that pathologic changes in the lung such as fibrosis or remodeling of the airway wall - both of which can serve to restrain airway wall motion - have the potential to increase wall shear stress and thus can form a positive feed-back loop for the development of altered flow profiles and airway remodeling. These observations are particularly interesting as we try to understand flow and structural changes seen in, for instance, asthma, emphysema, cystic fibrosis, and interstitial lung disease.

Keywords

human airway bifurcation; fluid-structure interaction; secondary flow; parenchymal tethering; wall shear stress

INTRODUCTION

The bronchial airways are compliant structures that change in dimension during breathing. Their change in dimension is determined by the composition of the airway wall and the mechanical properties of the wall constituents, tethering of the airway to the surrounding parenchymal tissue, and transmission of lung surface expanding forces through the tissue to the airway. Because the structure and the material properties of the airway wall differ from the surrounding lung tissue, the airway does not behave like a hole in the parenchyma[19]. The uppermost airways have a higher proportion of cartilage than those that are more peripheral,

[†]Corresponding author: Ching-long Lin, ching-long-lin@uiowa.edu, Tel: +1 319 335 5673.

and they are proportionately stiffer[59]. While the airways are known to deform with a change in lung volume, they have generally been assumed to be rigid structures in numerical studies that compute air pressure and flow[3, 30, 57]. This is in contrast to numerical studies of blood vessel perfusion, where the interaction between transmural pressure and the mechanics of the compliant vessel wall have been considered in several studies[41, 49, 56]. A major difference between systemic blood vessels and bronchial airways (or pulmonary vessels) is that the systemic vessels are usually surrounded by a relatively incompressible tissue (for example, cardiac or skeletal muscle), whereas the pulmonary airways and vessels are tethered to a very compliant and compressible tissue that is typically under tension and undergoes large strain during normal breathing. The systemic vessels experience relatively smaller strains during normal function than those of the breathing lung; the interaction between transmural pressure and bronchial airflow is therefore potentially significant, yet the validity of the assumption of airway rigidity for the study of bronchial airway pressure, flow, and particle transport has not previously been addressed. This leads to the first scientific question to be considered in the current study: what are the differences between the flow structures in the rigid and the compliant airway?

A viscous fluid exerts a shear stress on a surface over which it passes. The effect of shear in the circulation is readily seen as vasodilation in response to nitric oxide release from vascular endothelial cells that experience high local shear stress[36, 38]. In contrast to the blood vessels, transmission to, and the effect of, airflow induced shear stress on the airway wall is not yet understood, however it has been proposed that it may play an important role in the regulation of airway surface liquid[48] and mucociliary clearance via the regulation of ciliary beat frequency[42]. Airway wall shear stress has been estimated as relatively constant throughout the normal airway tree, using an idealized model of the airway tree and the assumption of a uniform distribution of flow[48]. In recent work, Lin *et al.*[28,29] simulated the turbulent laryngeal jet in the human airways using both direct numerical simulation and large-eddy simulation (LES) on TeraGrid clusters, in a realistic computational model of the human upper and intra-thoracic airway based on multi-detector computed tomography (MDCT) and geometry reconstruction techniques. They found that the wall shear stress induced by the turbulent laryngeal jet increases three fold in comparison to the case in the absence of the jet. This suggests that airway wall shear stress in the uppermost airways may be significantly larger than has previously been estimated using simplified models. This leads to the second question that will be considered in the current study: how does the assumption of rigidity affect the estimation of airway wall shear stress exerted by the flow on the airway wall?

This paper studies respiratory flow through an MDCT-based model of a single airway bifurcation and flow interaction with the airway walls with and without lung parenchymal tethering. A 3D time-accurate fluid-structure interaction (FSI) technique is used. This technique is based upon the Arbitrary Lagrangian-Eulerian (ALE) methodology and is composed of a structural dynamics solver and a fluid dynamics solver, which are coupled through a dynamic mesh algorithm[61].

METHODS

Mathematical formulation for the air

The governing Navier-Stokes equations for the incompressible viscous flow in an ALE framework for the FSI read:

$$\frac{\partial u_i}{\partial t}+(u_j-\tilde{u}_j)\frac{\partial u_i}{\partial x_j}=-\frac{1}{\rho}\frac{\partial p}{\partial x_i}+\frac{\partial}{\partial x_j}(\nu\frac{\partial u_i}{\partial x_j}) \quad (1)$$

$$\frac{\partial u_j}{\partial x_j}=0 \tag{2}$$

where u_i, p, ν and ρ are the air velocity, pressure, kinematic viscosity, and density respectively; $\tilde{u}_j$ is velocity of the fluid mesh and $u_j - \tilde{u}_j$ represents the ALE convective velocity induced by the difference between the air velocity and the mesh velocity. The subscript i is a free index and the repeated index j invokes Einstein summation.

Mathematical formulation for the structure

The governing equation for a continuum undergoing motion is given by Cauchy's equation in three dimensions[60, 61]:

$$\rho\frac{\partial v_i}{\partial t}=\nabla\cdot\sigma_{ij}+f_i \tag{3}$$

where the subscript i is a free index as before, f_i is the external force, and v_i is the velocity of the structure. The constitutive relationship between stress and strain is the generalized Hooke's law.

Fluid structure interaction

The current FSI system is treated as a triple-domain problem including the fluid domain, the structure domain, and the moving mesh, in which the governing equations are solved in an iterative manner. The Navier-Stokes equations are solved first for the fluid domain and then the fluid forces are computed on the structure surface. The dynamics equation is then solved for the structure under the influence of fluid forces, which provides deformation and velocity boundary conditions at the fluid-structure interface. The fluid mesh is moved by the dynamic mesh algorithm in accordance with these boundary conditions, which updates the mesh deformation and ALE velocity for the computation of fluid domain for the next time step. At the fluid structure interface, the two meshes are conformed to each other, i.e. the fluid mesh coincides with the solid mesh at the interface. Thus the information about mesh deformation, velocity and the fluid pressure is exchanged through this interface. The construction of the FSI method is implemented by coupling a computational fluid dynamics (CFD) solver[27] with a computational structural dynamics (CSD) solver[60, 61]. The two component solvers can be substituted with any other similar-functioned CFD and CSD solvers for various FSI phenomena. For model validation, please refer to the Appendix.

Model parameters

A realistic human airway model[2, 15, 17, 37, 50, 51] shown in Figure 1 is used in the current work. The detailed procedure to process the airway model can be found in Reference [28], in which the same model was analyzed to study the effect of the turbulent laryngeal jet on the airflow in the central airways. In this work, we choose to simulate the airflow and the airway wall motion in a typical two-generation bifurcation extracted from the CT-resolved airway tree. The section is taken from the 3rd–4th generations of the airway tree as highlighted in Figure 1. The reasons for choosing the 3rd–4th bifurcation in the current study are the following. First, the airways are not close to the trachea where the turbulence effect is significant. At the 3rd–4th airway bifurcation the turbulence intensity is about 5%[28]. The effect of turbulence on the airflow is limited, thus we can focus on the influences of fluid-structure interaction on the shear stress distribution. Second, the airway wall of this generation is more flexible than the trachea and main bronchi, resulting in a more

pronounced FSI phenomenon. Table 1 presents its geometric parameters. The ratio between the average diameters of the two lower branches is 1.38, corresponding to an area ratio of 1.96. The fluid mesh has 91,348 tetrahedral elements and the structural mesh has 75,853 tetrahedral elements. The inlet face of the upper branch and the outlet faces of the two lower branches are fixed in space, so the axial movement of the airway and the radial deformation at these faces are restrained.

The simulations are carried out for a normal breathing rate with a time period of T=4.8 seconds, i.e., 12.5 breathing cycles per minute. A sinusoidal parabolic velocity profile is imposed at the inlet of the 3rd generation (upper branch). The typical Reynolds number in the 3rd and 4th generations is on the order of hundreds[40]. The mean velocity at the inlet is derived from the flow rates measured at the same location in the whole CT-resolved airway simulation with the rigid airway wall[28]. Three mean velocities of 0.28 m/s, 0.57 m/s, and 1.47 m/s are chosen to represent different breathing efforts or flow conditions in the airways. The flow rates at the mouth associated with these three mean velocities are approximately 157 ml/s, 320 ml/s and 828 ml/s. The corresponding Reynolds numbers, $Re=\frac{\rho_{air}\overline{DU}}{\mu_{air}}$, in the upper branch are 90, 183, and 475, where the mean diameter of the inlet $\bar{D}$ is 4.85×10^{-3} m, the density of air ρ_{air} is 1.2 kg/m^3 and the viscosity μ_{air} is 1.73×10^{-5} N/s·m^2. The alveolar pressure during a breathing cycle follows approximately a sinusoidal wave with amplitude of about 1.1 cmH_2O[59]. The pressure drop from the 4th generation to the alveoli varies between 0.02 and 0.2 cmH_2O with a peak flow rate varying between 10 and 100 l/min, i.e. 167 and 1,667 ml/s[39]. Given the flow rates under consideration that are close to the lower bound of the above range, a sinusoidal pressure wave with amplitude of 1.0 cmH_2O shown in Figure 2(A) is imposed as a “reference” pressure at the two outlets of the airway model. A negative (positive) pressure corresponds to an inspiratory (expiratory) phase.

The airway is a very complex structure in terms of its composition and material properties. It consists of different layers of tissues with quite different functions and properties[48]. The airway motion is subject to the influence of two elastic structures: the airway itself and the surrounding parenchyma[19], which further complicates the analysis and computation. During ventilation, expanding forces are transmitted to the airway via tethering of the parenchyma to the outer airway wall. Different models have been proposed to estimate the tethering forces. For example, Mead *et al.*[32] adopted an elastic spring network to represent the parenchyma, Lambert and Wilson[25] used a linear continuum mechanics model to compute the tethering pressures, and later Lai-Fook[23, 24] proposed a nonlinear continuum mechanics model to compute the large parenchyma deformation for a contracting airway. To investigate the influence of the parenchymal tethering, we first compute the case using an airway bifurcation without tethering pressure and then adopt a sinusoidally interpolated tethering pressure ranging from −5 (~FRC) to −7.5 cmH_2O (~FRC + tidal volume) to represent the parenchymal tethering for normal breathing. According to the tethering pleural pressure profile for normal breathing[59], the parenchymal tethering pressure can be approximately expressed as (see Figure 2(B)):

$$p_{tet}=-5.0+1.25\times\left[\cos\left(\frac{2\pi}{T}t\right)-1\right]\ \text{cmH}_2\text{O} \tag{4}$$

where P_{tet} is the parenchymal tethering pressure, t is the time and T is the breathing period. As will be discussed later, the pressure variation due to flow in the airway model is much smaller than the reference pressure imposed at the outlets of the lower branches. By approximating the fluid pressure with the reference pressure, the resulting stress acting on

the airway wall can be estimated as shown in Figure 2(B), which is consistent with the known physiological condition in the human lungs[59].

The property of the airway wall is assumed isotropic. The density of the airway wall is taken as the density of muscle[16]: 1.04×10^3 kg/m^3. West and Matthews[58] measured the Poisson's ratio of excised dog lungs and gave an average value of 0.3. We tested a range of 0.2–0.49 for the Poisson's ratio and chose 0.4 for the simulation to reflect the relative incompressibility of the studied airway bifurcation. There are few published experimental data about the elastic properties of the airway walls. Codd *et al.*[10] reported that the average Young's moduli of tracheal tissue strips are 3.3 kPa and 9.3 kPa in the respective circumferential and axial directions. These parameters yield a very small deformation of the airway in the simulations. That is consistent with the notion that the trachea is relatively stiff and undergoes only small volume changes during tidal breathing. The section of the airway tree under consideration is a distal bronchus bifurcation, and therefore is expected to be more compliant than the trachea. The Young's modulus was selected by comparing the computed airway deformation with the average diameter change from functional residual capacity (FRC) to total lung capacity (TLC) measured from CT images. The *in-vivo* CT measurements of the airway were made by Saba[45], in which 41 healthy non-smokers were scanned in the supine body postures at two or three static volumes. 17 subjects were male and 24 were female, with ages ranging from 20 to 60 years old. The airways of these 41 subjects were segmented and the lung-volume-based changes in geometric measures were analyzed. A range of Young's modulus from 100 Pa to 3.0 kPa was tested in the FSI simulation of the flexible airway with tethering at Re=183; a value of 1.0 kPa was determined to best represent the deformation of the bifurcation. For the current subject, the total air volumes are 3.35 liter and 6.22 liter at FRC and TLC, respectively. The FRC volume is about 50% of TLC. Because the simulated FSI process is dynamic, we define the maximum volume registered during one cycle in the FSI results as "TLC". "FRC" is defined as the time instant when the volume is 50% of the maximum value at "TLC". Table 2 presents the computed geometric changes using the Young's modulus of 1.0 kPa. The percentage changes of these geometrical parameters together with the measurement data of Saba[45] are tabulated in Table 3. The current FSI-predicted airway deformation agrees well with the CT measurements as expected. Furthermore, the bifurcation angle of the current airway model changes little during the breathing cycle (62.3° at "FRC" and 63.5° at "TLC"). This is also consistent with Saba's measurement results, where the mean values of the branching angle were almost constant from FRC to TLC.

RESULTS

Flow in rigid airway

Before investigating the effects of the compliant airways on the airflow, the respiratory flows in the rigid airway bifurcation model are computed for the purpose of comparison. The airway is set to be 'rigid' by using a very large Young's Modulus E. The velocity profiles at inspiration and expiration phases in the plane of bifurcation are shown in Figures 3 and 4 (left panel). During inspiration, the airflow in the upper branch splits at the bifurcation and enters the two lower branches. Due to the inertia force, the faster-moving air tends to keep its moving direction and impinges on the inner walls of the bifurcation, while the slower-moving air is pushed towards the outer walls[40], inducing secondary counter-rotating vortical flows. The secondary flow forms skewed velocity profiles in the lower branches as shown in the velocity profiles at stations S_3 and S_5 (marked in Figure 3(A)), where the higher axial velocity is skewed toward inner walls. For expiratory flow, the airstreams in the two lower branches converge after the bifurcation in the upper branch, and the two converging airstreams generate secondary vortices in the upper branch due to the bifurcation curvature. It is observed that there is a dip in the velocity profile at station S_2 just

downstream of the bifurcation; this is soon transformed into a velocity peak at station S_1 (see the left panel in Figure 4). This is because the secondary flow motions sweep the slow-moving air between the two converging flows towards the outer wall.

The maximum magnitude of the wall shear stress in the rigid airway is about 0.055 and 0.03 Pa as shown in Figures 5(A) and 6(A) at respective peak inspiration and expiration. The time history of the maximum shear stress is presented in Figure 7. During the inspiration phase, the high shear stress occurs near the bifurcation and the outlets of the lower branches as depicted in Figure 5(A). The low wall shear stress is found at the middle section of the upper branch. The high shear stress behind the bifurcation is induced by the flow splitting, which consequently produces secondary vortices in the lower branches and increases the magnitude of the shear stress. The high shear stress near the outlets is caused by the narrowing of the airway lumen of the lower branches, which increases the average velocity and thus increases the strain rate of the air velocity. In contrast, the low shear stress region in the upper branch is caused by the area expansion of the airway lumen before the bifurcation. During the expiration phase, the high shear stress near the bifurcation observed at inspiration disappears and the low shear stress is found in front of the bifurcation in the upper branch as shown in Figure 6(A). Further downstream toward the boundary face of the upper branch, a local maximum stress is formed. This is because the high-speed air streams coming from the two lower branches merge in the lumen of the upper branch away from the wall as indicated by the dip of the velocity profile at station S_2 in Figure 4.

Flow in compliant airway without parenchymal tethering

With a flexible airway wall, a considerable deformation of the airway can be observed in a breathing cycle as illustrated in Figure 8. Figure 8(A) overlays the airway lumens at the resting state (solid gray) and the inspiration phase (wireframe black), and Figure 8(B) shows the inner faces of the airway wall at these two states. During inspiration, the transmural pressure drives the airway to expand in the direction along A-A′ in Figure 8(C), which is perpendicular to the bifurcation plane, and contract along B-B′ in parallel with the bifurcation plane. This is because the cross section of the airway before the bifurcation exhibits an elliptical shape having a larger diameter in the direction parallel to the bifurcation plane, thus the airway walls near A and A′ in Figure 8(C) have a larger area than those near B and B′, experiencing larger fluid forces and dominating the direction of the motion of the airway wall. When the airway contracts along B-B′ during inspiration, the curvature of the outer wall is increased as shown in Figure 8(B), which subsequently influences the airflow characteristics.

Figures 3 and 4 (right panel) show the velocity profiles during inspiration and expiration at Re=90, 183, and 475 with elastic airway walls. During inspiration, the airway motion induces a slow-moving air region near the wall in the upper branch as circled in the velocity profiles at station S_2 in Figures 3(B) and 3(C). The slow-moving region expands almost to the center of the lower branches at Re=475, producing a more concentrated velocity profile at S_2. The bending curvatures of the outer walls increase during inspiration as the airway deforms, so the air in the upper branch needs to turn a sharper angle to enter the lower branches, subsequently strengthening the secondary flow motions in the lower branches. Figure 9 compares the velocity profiles along the dashed line in Figure 3(A) where the maximum shear stress is approximately located in both rigid and compliant airway models. At Re=90, the wall deformation is relatively small and the bending curvature is slightly increased, so the effects of wall motion on the airflow distribution is not evident. Only small differences appear in the velocity profiles in both rigid and compliant airway models as shown in Figure 9(A). While at Re=183 and Re=475 with larger airway deformations, the velocity profiles in the lower branches are greatly influenced by the strengthened secondary flows. The velocity profiles in the compliant airway are more skewed towards the inner wall

than those in the rigid airway as presented in Figures 9(B) and 9(C). During expiration, the velocity profiles are quite similar to those with rigid walls and the wall motion does not have much influence on the expiratory flow. This is probably because secondary flow motions in the upper branch are induced by the converging streams from the two lower branches and the pattern of the secondary flow is primarily determined by the branching angle of the bifurcation which changes little during inspiration and expiration.

The wall shear stress distribution with the flexible airway wall is presented in Figures 5(B) and 6(B). During inspiration, the airway wall expands and induces a larger region of slow-moving air near the airway wall as shown in the velocity profiles of Figure 3 (marked by circles), leading to a smaller wall shear stress on the airway wall. The magnitude of shear stress reduces almost 5 fold compared with the shear stress distribution on the rigid airway. The high shear stress regions are still found at the bifurcation and near the outlets of the lower branches, but their magnitudes are smaller compared with those on the rigid airway. The low shear stress region in the upper branch has a larger area with the expanded airway lumen. During expiration, the wall shear stress on the flexible airway wall is also smaller than that on the rigid airway wall.

Flow in compliant airway with parenchymal tethering

The lung parenchyma is an elastic structure and its mechanical properties contribute to maintain the patency of the airway lumen, and to expand the airway during inspiration. The parenchymal tethering pressure is added to the structural dynamics solver as an external force in Eq. (3). To investigate the influences of the tethering on the airflow characteristics, the FSI method is applied to simulate the same airway bifurcation model with tethering at *Re*=183. Figure 10(A) compares the airway wall deformations in the models with and without lung parenchymal tethering. With the parenchymal tethering the airway wall attains a larger deformation due to the pulling effect of the tethering pressure, whereas with increasing airway rigidity the deformation is restrained. Figure 10(B) compares the velocity profiles for the cases of the rigid airway, the flexible airway, and the flexible airway with tethering at peak inspiration. It shows clearly that the velocity gradient in the wall normal direction at r/R= 1 near the bifurcation decreases due to the flexibility of the airway and parenchymal tethering. A decrease in velocity gradient reduces wall shear stress. The locations of the maximum shear stresses at peak inspiration for these cases are about the same near the bifurcation as shown in Figure 5. At peak expiration, the local maximum stresses are found near the boundary faces in the lower branches and downstream in the upper branch. Like inspiratory flow, these stresses decrease with airway compliance and tethering.

DISCUSSION

The roles of mechanical forces in lung function and pathophysiology

The wall shear stress generated by airflow in the airways is known to alter cell shape and elicit biologically relevant signals. For instance, Dailey *et al.*[11] studied wall shear stress distribution on airway epithelial cells, and found that more flexible epithelial cells experience lower wall shear stresses. The cell deformation can mitigate shear stress amplification. Sidhaye *et al.*[46] found that low levels of luminal shear stress generated by airflow can regulate and enhance airway epithelial barrier function that protects against inhaled infectious bacteria and inflammatory particles. Tarran *et al.*[48] and Button and Boucher[8] showed that airway defense appears to be related to the phasic motion of pulmonary ventilation via shear stress-induced adenosine triphosphate nucleotide (ATP) release. Button *et al.*[7, 8] further demonstrated that cyclic compressive stress, resembling stress observed in the lung during tidal breathing, increases the ATP release rate onto the

surface of the airway. The elevated ATP concentration subsequently stimulates liquid secretion and acceleration of mucociliary clearance, which promotes lung health. Tschumperlin *et al*.[52, 53] also found in cell culture experiments that the compressive stress exerted on human bronchial epithelial cells regulates pro-fibrotic pathway signaling. The stress was generated by an apical-to-basal transcellular pressure difference comparable to that found in the airway during bronchoconstriction. It is noted in the current study that at peak inspiration the fluid (reference) pressure at the outlets of the two lower branches is −1 cmH_2O (−98 Pa), but the pressure difference between the inlet and outlets of the three airway models at peak inspiration for Re=183 and 475 varies ~0.5–2 Pa and the maximum pressure found at the bifurcation is only ~1–5 Pa higher than at the outlets.

Thus, the deviation of overall fluid pressure from the reference pressure at the outlets is small (less than ~5%). Furthermore, the maximum normal stress is also found near the bifurcation and has a similar range of magnitudes as the maximum shear stress, ~0.005–0.05 Pa. Given the tethering pressure expressed in equation (4), the resulting stress acting on the airway wall can be approximated by the dot-dashed line in Figure 2(B) and is up to ~ −8 cmH_2O. The current ranges of the shear stress and the resulting stress agree with the relevant physiological ranges of stress amplitudes reported by Button *et al*.[8] (up to 0.5 dynes/cm^2=0.05 Pa for shear stress and 8.5 cmH_2O for compressive stress). Whether the resulting stress functions similarly to the compressive stress or the transcellular pressure difference produced in the cell culture experiments requires further investigation. Nevertheless, the above analysis suggests that the compressive stress might depend more on parenchymal tethering than fluid stress and the relationship between airway function, stress, and airway rigidity needs further study.

In the study of asthmatics via the Severe Asthma Research Program (SARP), Fain *et al.*[12] analyzed MDCT images of 118 human subjects with asthma (58 severe, 35 non-severe, and 25 normal controls), and found that across all airway segments there was significant increase in the airway wall thickness and the lumen eccentricity in subjects with severe asthma compared with non-severe cases. The remodeling of the airway in asthmatics, or the stiffening of lung tissue in pulmonary fibrosis, serves to restrain the motion of the airway and leads to a higher wall shear stress on the surface. The elevated wall shear stress may damage the airway epithelial layer, making the airway more prone to further pathologic events, thus establishing a vicious cycle of events.

The study of the effects of tethering forces on airway motions is also important in understanding lung pathophysiology because localized change in tissue stiffness (or compliance) occurs during development and progression of lung diseases, such as chronic obstructive pulmonary disease (COPD) or interstitial pulmonary fibrosis (IPF). The current results show that the tethering forces pull the airway wall to prevent airway closure, and subsequently achieve larger airway deformation and lower wall shear stress. This study implies that tissue degeneration in the lungs has the potential to increase wall shear stress and contribute to airway rigidity. There is increasing evidence of airway remodeling associated with patients who have emphysema[21]. The FSI studies may therefore provide new insights into site-specific airway changes in lung diseases.

The effects of airway motion on wall shear stress

If the airflow is assumed to be laminar with a parabolic axial velocity profile, the maximal peak wall shear stress can be estimated as,

$$\tau_w = \frac{32\mu Q}{\pi d^3} \quad (4)$$

where d is the diameter of the airway, Q is the flow rate and μ is the viscosity. Tarran *et al.*[48] calculated the wall shear stress based on this equation and gave estimates for the whole airway tree. They predicted that the wall shear stress varies little with airway order, from a minimum value of 0.019 Pa in the trachea (generation 0) to a maximum of 0.073 Pa at generation 8 (see Figure 4a and supplemental material in Ref. [48]). Nucci *et al.*[33] reported similar results. The current airway bifurcation is between the 3rd and 4th generations, for which Tarran *et al.*[48] reported the values of 0.043 Pa and 0.04 Pa, respectively. It is worth noting that the airway is assumed rigid in equation (4) because the diameter of the airway is constant. The current shear stress calculated based upon the rigid bifurcation model is 0.055Pa, which agrees well with the literature.

By assuming that the airway diameter increases by 25% due to airway expansion (see Table 3), the above formula (4) predicts that the wall shear stress reduces by about 50%. Nonetheless, in the current FSI study, with an elastic wall without tethering, the maximum wall shear stress is decreased 80% from 0.05 Pa (for the rigid airway) to 0.01 Pa as the luminal space enlarges. With addition of the parenchymal tethering force, the wall shear stress is further mitigated 50% to about 0.005 Pa. The shear stress ratios measured at the same locations in the three cases (rigid airway: flexible airway: flexible airway with tethering) vary with the luminal area and the airway wall velocity registered at that location. For example at S2 marked in Figure 3(A), the shear stress ratio for the three cases is ~3.2:2:1, while near the bifurcation the ratio is ~10:5:1. It is noteworthy that the latter high ratio is based on the instantaneous shear stress which is localized near the bifurcation at peak inspiration. Thus, we shall also comment on the change of the bulk airway resistance of the airway bifurcation model. At peak inspiration with Re=183, the pressure drops between the inlet and outlets of the airway model are about 1.2, 0.75 and 0.44 Pa for the cases of the rigid airway, the flexible airway, and the flexible airway with tethering, respectively. Since the flow rates for these cases are the same, the ratio of the airway resistance, viz. the ratio of pressure drop over flow rate, is 2.7: 1.7: 1. This ratio is much smaller than that of the local peak shear stress, indicating that the high stress is a localized event. Whether the onset of airway disorders is associated with localized abnormal high shear stress deserves further study.

In the above analysis, we treat the compliant airway with tethering as the normal functional airway. It is important to note that, before the addition of tethering pressure, the compliant airway geometry represents a static airway that is in equilibrium with a non-zero tethering pressure, and the additional tethering pressure that we apply shifts the airway away from FRC. The model analysis should therefore not be interpreted as quantitatively representative of the exact *in vivo* airway deformation, but rather as an approximation that allows us to compare the three cases (compliant with tethering, compliant without tethering, and rigid) using consistent initial geometries and boundary conditions. The Young's modulus that we use is an approximation for the elasticity of the airway as it expands from FRC to TLC under the influence of *in vivo* tethering pressures. The dimension of the airway for the compliant airway case is larger than that of the rigid airway case because of relaxation of Young's modulus used in the rigid model and imposition of transmural pressure. A question arises as to what the maximum shear stress would be in the rigid airway whose size is about the same as the compliant airway with tethering. To answer this question, we applied a constant tethering force of -5 cmH_2O to enlarge the airway and used it for the rigid airway simulation. The maximum shear stress found in this case is 0.03 Pa, which is about six times

greater than the peak stress 0.005 Pa found in the compliant model with tethering. This suggests that depending on the type and state of lung disease, the diameter of the rigid airway can be either smaller than or about the same as the normal one, resulting in different levels of stress increase that are between 6–10 fold. Also, we ran a compliant airway case with the tethering force ranging from 0 to −2.5 cmH_2O, which yields the maximum shear stress of 0.0073 Pa. This stress falls between those found in the case without tethering and the case with tethering ranging from −5 to −7.5 cmH_2O. It suggests that with a smaller tethering force the airway registers smaller deformation (than the case with the maximum tethering pressure of −7.5 cmH_2O), thus a larger maximum shear stress.

The reduction of the wall shear stress in the compliant airway cases is attributable to the enlargement of the airway luminal space and the motion of the airway wall. The enlarged airway luminal space reduces the mean velocity of the airflow, which subsequently reduces the wall shear stress. Figure 11(A) presents the area change of the upper airway at peak inspiration, and Figure 11(B) overlays the axial velocity profiles for the three cases (rigid airway: flexible airway: flexible airway with tethering). Taking section S3 for example, the cross-sectional area of the rigid model at this location is 21.5 mm^2. For the flexible model, the area is 26.8 mm^2, which is 25% larger than the rigid one. And for the flexible model with parenchyma, the area is 34.7 mm^2, 62% larger than the rigid one. The ratio of the three areas is 1.00:1.25:1.62, so the ratio of mean velocities is 1.0:0.80:0.62. The maximum reduction in the shear stress occurs at peak inspiration when the airway wall velocity also reaches its maximum value. Let Q_D denote the volumetric flow rate at the inlet of the upper branch and Q_w the rate at which the airway wall draws the airflow to fill the enlarged luminal space at inspiration. The ratios of Q_w/Q_D at peak inspiration are 0.18 and 0.35 for the flexible airway and the flexible airway with parenchyma tethering, respectively. A large Q_w/Q_D value can cause an adverse pressure gradient along the flow direction in the airways and retard the flow in the wall region[55]. A comparison of the pressure distributions in the upper branch for the cases of rigid airway, flexible airway, and flexible airway with tethering, shows that the pressure gradient in the rigid airway at peak inspiration is negative (favorable), whereas it becomes positive (adverse) in the other two cases. Tsuda *et al.*[54] reported that Q_w/Q_D is an important parameter in determining the characteristics of the alveolar flow in a rhythmically expanding and contracting alveolated duct. Uchida and Aoki[55] analytically studied unsteady flows in a semi-infinite contracting or expanding pipe and found that in an expanding pipe the flow adjacent to the wall is highly retarded and eventually reversed at a high Reynolds number. The non-zero velocity of the airway wall near the bifurcation at r/R=1 (the inner wall) in Figure 9(B) may also contribute to the reduction of the maximum wall shear stress because it is almost parallel to the inspiratory airflow in the upper branch. As a result, the relative velocity of the airflow toward the bifurcation is smaller than the airflow velocity, leading to smaller shear stress.

In the study of blood flow, Anayiotos *et al.*[1] found experimentally by laser Doppler velocimetry that vessel compliance reduced the mean wall shear rate level by about 30% at most locations as compared with the rigid wall model. And the effect of compliance was more significant on the instantaneous maximum and minimum shear stresses, which could be reduced by as much as 100% in the compliant model. Kim *et al.*[22] reported similar findings in the wall shear stress distribution in rigid and compliant blood vessels using the FSI approach. Ye and Bull[62] studied numerically the expansion of a microbubble in a liquid-filled flexible tube for potential treatment of tumors by using acoustic vaporization of intravascular perfluorocarbon droplets to damage blood vessels. They found that wall flexibility can significantly affect the wall stresses resulting from vaporization of droplets. The conclusions of these studies are consistent with the current study: that airway compliance affects wall shear stress.

Comparison with in-vivo measurement and pressure-area curves

Brown *et al.*[5, 6] measured the airways in dogs and sheep by means of high-resolution CT and reported the magnitude of the airway distension in dogs during a methacholine challenge for a transpulmonary pressure ranging from 0 to 25 cmH_2O. As compared with the pressure range investigated here, i.e. 4.6–8.0 cmH_2O, our simulation conditions are consistent with Brown *et al.*'s measurements.

The relationship between transmural pressure and normalized cross-sectional areas of the compliant airway with tethering pressure predicted by the FSI is plotted in Figure 12. In this work, the transmural pressure ranges from 4.6 to 8.0 cmH_2O as seen in Figure 2(B). The negative sign in Figure 2(B) means the pressure difference points outwards to the airway, so the transmural pressure is positive. The cross-sectional areas are normalized by the maximum areas, and the pressure-area curve is plotted for the range between 4.6–8.0 cmH_2O to compare with the pressure-area curve derived by Lambert *et al.*[26]. Good agreement is observed for the pressure range under investigation.

The assumption of isotropy and linear material properties

The current model uses the simplifying assumptions of a single Young's modulus, isotropy of the airway and lung tissues, and linear elasticity for the airway stress-strain behavior. The implication and validity of these assumptions are discussed below.

The Young's modulus E=1 kPa of the airway wall used in the above study was estimated by fitting with CT measurements. This modulus may not be representative of airway disorders. To assess the sensitivity of peak wall shear stress to wall rigidity for the functional relationship over a physiological range, we tested a series of Young's moduli ranging between 0.1 and 100 kPa using the flexible airway model with tethering. The E value (kPa) and the corresponding maximum shear stress (Pa) are: (0.1, 0.0012), (0.5, 0.0026), (1, 0.005), (5, 0.014), (10, 0.035), (50, 0.047), (100, 0.05). The results show that with an E value of greater than 10 kPa the peak stress approaches an asymptote with increasing E. Thus, the airway having an E value in that range could be approximated as rigid. However, the actual stress should also depend on the tethering force of the diseased state of the lung, which is unknown and requires further investigation.

In the current work, the airway and surrounding lung parenchymal mechanics are assumed isotropic, which means that the lung tissues are homogeneous and deform uniformly in all directions. However the composition of the real airway wall and the lung tissue are inhomogeneous. Sinclair *et al.*[47] demonstrated that the airway expansion in rats during mechanical ventilation is anisotropic. They also noted that the anisotropy is more prominent at large deformations of 60%–80% strains. This is much larger than the deformation studied in this work, which is usually less than 20%. Material that is expanded non-uniformly becomes anisotropic at reasonably large strains. Ranford[43] showed that strips of lung tissue cut from lungs in different orientations have approximately the same length-tension characteristics. In addition, Rohrer[44] found that ink circles stamped on the pleural surfaces of excised lobes maintained their shape as the lobes were deflated over a large volume range. The latter two studies suggest that the airway may behave isotropically at small strains despite their heterogeneous composition. The behavior of the real lung tissue when the strain in one direction exceeds that in another direction is not known, and to what extent anisotropy will be present is not yet quantified, so the error of the current model associated with the assumption of isotropic tissue properties cannot be assessed.

Many studies[13, 14, 34] have shown that the lung and its composing tissues deform in a nonlinear manner. Experimental results on rat lungs by Sinclair[47] showed that the airway wall tension increased rapidly when the strain reached a certain level, suggesting there is a

'strain limit' for the airway wall. Ranford[43] also showed that the stress increased sharply when the lung tissue was stretched by about 80% of its original resting length. Based on Ranford's results, West and Matthews[58] derived a nonlinear Young's modulus model $E=0.8E_0/(0.8-\varepsilon)$ for their numerical simulation, where E_0 is the modulus at resting status and ε is the strain. Mead *et al.*[32] also proposed similar equations for the nonlinear response of the lung tissue. It would be more physically accurate to adopt nonlinear elasticity for the airway, but it is also noteworthy that the nonlinearity is most pronounced when the strain is of the order of 60%–80%. The CT images show that the deformation of the airway bifurcation between the 3rd and 4th generations is less than 20%[45], see Table 3, so the linear elasticity model is adopted here. Noble *et al.*[35] suggested that the parenchymal elastic after-loads do not restrict the airway narrowing in mid-sized cartilaginous bronchi. In this work, the parenchymal tethering pressure is included in the model to consider all the possible mechanical loads acting on the airway wall. Whether the parenchymal elastic after-loads are significant in the airway wall motion or not is determined by the airway deformation. Viscoelastic properties are not included in the current model because with only less than 20% deformation in the central airway the airway wall may be mostly elastic. Since the aforementioned studies focused on animal data with small lungs or on lung surfaces, the applicability of these data to large airways in humans as in the current study requires further validation.

The effects of turbulence, mesh size, boundary and initial conditions

In the whole airway simulation, the turbulent laryngeal jet was formed when the upper airway geometry was included in the simulation[28]. Without the upper airway, the turbulent laryngeal jet was absent, and thus the flow became laminar as in van Ertbruggen *et al.*[57]. The maximum shear stress at the airway segment extracted for the current study is about 10% higher in the presence of turbulence[28]. The shear stress with and without turbulence is therefore of similar magnitude, indicating that the 5% turbulence intensity at the current bifurcation has limited effect on the shear stress distribution. Here the effect of turbulence on the shear stress distribution is further evaluated by comparing the simulation results obtained with and without turbulence. The turbulence effect is introduced by adding random perturbation of 5% turbulence intensity to the mean velocity imposed at the inlet of the compliant airway model. The LES model[9, 28] is adopted. The maximum shear stress calculated with the turbulence effect is about 7% and 10% higher than the laminar cases without and with tethering, respectively. The percentage differences are consistent with that computed from the whole airway simulation[28]. However, the shear stress variation caused by turbulence seems less significant as compared with the effect of elastic airways and lung parenchyma.

To assess the sensitivity of mesh size on maximum wall shear stress, two cases using coarse meshes of 42,384 and 86,775 elements for airflow in a rigid airway model were simulated, resulting in the maximum shear stresses of 0.048 and 0.053 Pa, respectively. As compared with the above fine mesh (91,348 elements) solution of 0.055 Pa, the difference in shear stress reduces from 12.7% to 3.6%, indicating that the current mesh is adequate to resolve the airflow near the wall region. Similar mesh-independence study has been performed on solid mesh. Generally, the fluid solver requires much finer mesh than the solid solver. Thus, by choosing the mesh size of the fluid solver for both fluid and solid domains (note that these two meshes are confirming at the interface), we can ensure that the solutions for the solid solver is also mesh-independent.

To assess the effect of inlet velocity profile on shear stress, we inspect the velocity profile at the current inlet location extracted from the whole rigid airway simulation. The velocity profile, although skewed, has largely recovered its parabolic shape. This profile is then imposed at the inlet of the current compliant airway model with tethering force for

simulation. The result is compared with those using the uniform and parabolic velocity profiles. For the three profiles, the regions of maximum wall shear stress are all located in the vicinity of the bifurcation, and the difference between the maximum shear stresses is less than 5%. Furthermore, the imposed sinusoidal velocity waveform has equal inspiration and expiration times, being different from a typical inspiration-expiration ratio of 1:2. Although the total expiration time also includes an expiratory pause, the longer expiratory time may affect the flow rate as well as the shear stress. Another limitation of this study is due to the pressure boundary condition imposed at the outlets of the lower branches. Ideally the boundary conditions should be inferred from pulmonary function tests or other sensitivity analysis of an actual patient. It is thus recommended that future work should impose a more realistic breathing waveform and a more accurate estimate of the boundary condition.

The clamped boundary condition for the solid solver imposed at the inlet and exit cross-sectional faces of the airway wall restricts axial and radial deformations of the airway at the inlet and outlet faces. To assess the error incurred by this constraint in axial deformation, image registration[63] was employed to register CT images at TLC and FRC to derive the displacement fields between them. The coordinates and the displacement fields for the nodal points at the inlet and exit cross-sectional faces of the airways were then used to estimate the axial deformation. Although this estimate is based upon static volume scans, the results show that the average axial deformation is about 5%, which is much smaller than radial deformation (Table 3). As for the error incurred by the constraint of radial deformation, it is recommended that future work should consider as many generations of airways as possible.

The effects of the airway surface liquid (ASL) layer lining the epithelium on wall shear stress are not considered in the current model. Because the shear stress is continuous at the air-liquid interface[20] and the bulk viscosity and density of the ASL are much larger than those of air, the mean velocity gradient in the ASL layer may be very small. Besides, the thickness of the ASL layer is on the order of 10 μm[6, 7], much smaller than the current airway diameter (4 mm) and thickness (1.5 mm), so its influence on the airflow velocity profile may be limited.

CONCLUSIONS

The respiratory flow in a human airway bifurcation with rigid and compliant airway walls has been investigated by using the 3D ALE-based FSI method. The airway model is a realistic replication based on MDCT data. The effects of airway wall compliance (rigid versus flexible walls) and the effects of lung parenchymal tethering have been investigated. The results show that the airway wall motion plays an important role in influencing the respiratory airflow patterns through a bifurcation. During inspiration the expansion of the compliant airway yields a larger airway lumen space, which subsequently produces flatter airflow velocity profiles near the bifurcation and substantially reduces the maximum wall shear stress. With increasing airway rigidity and/or weakening parenchymal tethering, the wall stress increases. The peak shear stress is found in the vicinity of the bifurcation. In the human lung, the periciliary liquid and mucus - together with trapped inhaled bacteria and particulates - are continuously transported cephalad by coordinated ciliary beating. The bifurcation is a singular point where the inner walls of daughter branches meet and toxins/irritants accumulate; this is therefore a key weak spot in the network of mucociliary transport. Whether the elevated high shear stress at the bifurcation due to pathologic changes in the lung would alter biochemical responses at the cellular level, disrupt mucociliary transport, and form a vicious feed-back loop for development of airway disorders is worth further study.

Acknowledgments

This work was supported in part by NIH Grants R01-HL-064368, R01-EB-005823, and S10-RR-022421. We are grateful to Jiwoong Choi and Youbing Yin for assisting with generation of meshes and CT images of the airway model. We also thank TeraGrid via the Texas Advanced Computing Center for allocating computer time.

References

1. Anayiotos AS, Jones SA, Giddens DP, Glagov S, Zarins CK. Shear stress at a compliant model of the human carotid bifurcation. ASME J Biomech Eng 1994;116:98–106.
2. Aykac D, Hoffman EA, McLennan G, Reinhardt JM. Segmentation and analysis of human airway tree from 3D X-ray images. IEEE Trans Med Imag 2003;22(8):940–950.
3. Balásházy I, Hofmann W, Heistracher T. Local particle deposition patterns may play a key role in the development of lung cancer. J Appl Physiol 2003;94:1719–1725. [PubMed: 12533493]
4. Bertram, CD. Experimental studies of collapsible tubes. In: Carpenter, PW.; Pedley, TJ., editors. Flow past Highly Compliant Boundaries and in Collapsible Tubes. Kluwer Academic Publishers; Dordrecht, The Netherlands: 2003. p. 51-65.
5. Brown RH, Mitzner W. Delayed distention of contracted airways with lung inflation *in vivo*. Am J Respir Crit Care Med 2000;162:2113–2116. [PubMed: 11112124]
6. Brown RH, Mitzner W, Wagner E, Permutt S, Togias A. Airway distension with lung inflation measured by HRCT. Acad Radiol 2003;10:1097–1103. [PubMed: 14587628]
7. Button B, Picher M, Boucher RC. Differential effects of cyclic and constant stress on ATP release and mucociliary transport by human airway epithelia. J Physiol 2007;580:577–592. [PubMed: 17317749]
8. Button B, Boucher RC. Role of mechanical stress in regulating airway surface hydration and mucus clearance rates. Resp Physio Neurobio 2008;163:189–201.
9. Choi J, Tawhai MH, Hoffman EA, Lin CL. On intra- and intersubject variabilities of airflow in the human lungs. Phys Fluids 2009;21:101901.
10. Codd SL, Lambert RK, Alley MR, Pack RJ. Tensile stillness of ovine trachea wall. J Appl Physio 1994;76:2627–2635.
11. Dailey HL, Yalcin HC, Ghadiali SN. Fluid-structure modeling of flow-induced alveolar epithelial cell deformation. Comput Struct 2007;85:1066–1071.
12. Fain SB, Peterson ET, Evans M, Granroth JC, Newell J, Hoffman E, Kuhlman JE, Jarjour N, Wenzel S, Castro M. The SARP network investigators. Airway abnormalities are localized to specific regions in severe vs. non-severe asthma. Am Thoracic Society International Conference Abstracts Issue, Am J Respir Crit Care Med 2008;177:A29.
13. Fung YCB. Elasticity of soft tissues in simple elongation. Am J Physio 1967;213:1532–1544.
14. Fust A, Bates JHT, Ludwig MS. Mechanical properties of mouse distal lung: *in vivo* versus *in vitro* comparison. Resp Physio Neurobio 2004;143:77–86.
15. Guo J, Reinhardt JM, Kitaoka H, Zhang L, Sonka M, McLennan G, Hoffman EA. Integrated system for CT-based assessment of parenchymal lung disease. IEEE International Symposium on Biomedical Imaging 2002:871–874.
16. Heil, M.; Jensen, OE. Flows in deformable tubes and channels: theoretical models and biological applications. In: Carpenter, PW.; Pedley, TJ., editors. Flow past Highly Compliant Boundaries and in Collapsible Tubes. Kluwer Academic Publishers; Dordrecht, The Netherlands: 2003. p. 15-50.
17. Hoffman EA, Gnanaprakasam D, Gupta KB, Hoford JD, Kugelmass SD, Kulawiec RS. VIDA: an environment for multidimensional image display and analysis. Proc SPIE: Med Imag 1992;1660:694–711.
18. Kamm RD, Pedley TJ. Flow in collapsible tubes: a brief review. ASME J Biomech Eng 1989;111(3):177–179.
19. Kamm RD. Airway wall mechanics. Annu Rev Biomed Eng 1999;1:47–72. [PubMed: 11701482]
20. Kang M, Fedkiw RP, Liu XD. A boundary condition capturing method for multiphase incompressible flow. J Scientific Comput 2000;15:323–359.

21. Kim WD, Sean HL, Harvey OC, John CE, John Y, Robert DL, Peter DP, James CH. The association between small airway obstruction and emphysema phenotypes in COPD. Chest 2007;131:1372–1378. [PubMed: 17317735]
22. Kim YH, Kim JE, Ito Y, Shih AM, Brott B, Anayiotos AS. Hemodynamic analysis of a compliant femoral artery bifurcation model using a fluid structure interaction framework. Ann Biomed Eng 2008;36(11):1753–1763. [PubMed: 18792781]
23. Lai-Fook SJ, Wilson TA, Hyatt RE, Rodarte JR. Elastic constants of inflated lobes of dog lungs. J Appl Physio 1976;40:508–513.
24. Lai-Fook SJ. A continuum mechanics analysis of pulmonary vascular interdependence in isolated dog lobes. J Appl Physio 1979;46:419–429.
25. Lambert RK, Wilson TA. A model for the elastic properties of the lung and their effect on expiratory flow. J Appl Physio 1973;34:34–48.
26. Lambert RK, Wilson TA, Hyatt RE, Rodarte JR. A computational model for expiratory flow. J Appl Physio 1982;52:44–56.
27. Lin CL, Lee H, Lee T, Weber LJ. A level set characteristic Galerkin finite element method for free surface flows. Int J Numer Meth Fluids 2005;49:521–547.
28. Lin CL, Tawhai MH, McLennan G, Hoffman EA. Characteristics of the turbulent laryngeal jet and its effect on airflow in the human intra-thoracic airways. Resp Physio Neurobio 2007;157:295–309.
29. Lin C-L, Tawhai MH, McLennan G, Hoffman EA. Multiscale simulation of gas flow in subject-specific models of the human lung. IEEE Eng Med Biol 2009;28(3):25–33.
30. Liu Y, So RMC, Zhang CH. Modeling the bifurcating flow in an asymmetric human lung airway. J Biomech 2003;36:951–959. [PubMed: 12757804]
31. Marzo A, Luo XY, Bertram CD. Three-dimensional collapse and steady flow in thick-walled flexible tubes. J Fluids and Structures 2005;20:817–835.
32. Mead J, Takishima T, Leith D. Stress distribution in lungs, a model of pulmonary elasticity. J Appl Physio 1970;28:596–608.
33. Nucci G, Suki B, Lutchen K. Modeling airflow-related shear stress during heterogeneous constriction and mechanical ventilation. J Appl Physio 2003;95:348–356.
34. Noble PB, Sharma A, McFawn OK, Mitchell HW. Elastic properties of the bronchial mucosa: epithelial unfolding and stretch in response to airway inflation. J Appl Physio 2005;99:2061–2066.
35. Noble PB, Sharma A, McFawn PK, Mitchell HW. Airway narrowing in porcine bronchi with and without lung parenchyma. Eur Respir J 2005;26:804–811. [PubMed: 16264040]
36. Oscar AP, Bryant MB, Panza JA. Role of endothelial nitric oxide in shear stress–induced vasodilation of human microvasculature: diminished activity in hypertensive and hypercholesterolemic patients. Circulation 2001;103:1752–1758. [PubMed: 11282906]
37. Palagyi K, Tschirren J, Hoffman EA, Sonka M. Quantitative analysis of pulmonary airway tree structures. Comput Biol Med 2006;36(9):974–996. [PubMed: 16076463]
38. Paszkowiak JJ, Dardik A. Arterial wall shear stress: observations from the bench to the Bedside. Vascular and Endovascular Surgery 2003;37:47–57. [PubMed: 12577139]
39. Pedley TJ, Schroter RC, Sudlow MF. The prediction of pressure drop and variation of resistance within the human bronchial airways. Respir Physio 1970;9:387–405.
40. Pedley TJ. Pulmonary fluid dynamics. Annu Rev Fluid Mech 1977;9:229–274.
41. Perktold K, Rappitsch G. Computer simulation of local blood flow and vessel mechanics in a compliant carotid artery bifurcation model. J Biomech 1995;28:845–856. [PubMed: 7657682]
42. Picher M, Burch LH, Boucher RC. Metabolism of P2 *r*eceptor *a*gonists in human airways: implications for mucociliary clearance and cystic fibrosis. J Biol Chem 2004;279:20234–20241. [PubMed: 14993227]
43. Ranford, EP. Recent studies of mechanical properties of mammalian lungs. In: Remington, JW., editor. Tissue Elasticity. p. 177-190.Am Physiol Soc. 1957
44. Rohrer F. Ueber die topographische verteilung der elastischen eigenschaften in der lunge. Schweiz Med Wochschr 1921;51:740–741.

45. Saba, OI. PhD Thesis. The University of Iowa; 2005. A characterization of normal human airway tree geometry *in-vivo* over multiple lung volumes *via* standardized methods for volumetric CT imaging.
46. Sidhaye VK, Schweitzer KS, Caterina MJ, Shimoda L, King LS. Shear stress regulates aquaporin-5 and airway epithelial barrier function. PNAS 2008;105:3345–3350. [PubMed: 18305162]
47. Sinclair SE, Molthen RC, Haworth ST, Dawson CA, Waters CM. Airway strain during mechanical ventilation in an intact animal model. Am J Resp and Critical Care Med 2007;176:786–794. [PubMed: 17626911]
48. Tarran R, Button B, Picher M, Paradiso AM, Ribeiro CM, Lazarowski ER, Zhang L, Collins PL, Pickles RJ, Fredberg JJ, Boucher RC, Matthews FL. Normal and cystic fibrosis airway surface liquid homeostasis: the effects of phasic shear stress and viral infections. J Biol Chem 2005;280(42):35751–35759. [PubMed: 16087672]
49. Taylor CA, Hughes TJR, Zarins CK. Finite element blood flow modeling in arteries. Comput Methods Appl Mech Engrg 1998;158:155–196.
50. Tschirren J, Hoffman EA, McLennan G, Sonka M. Intrathoracic airway trees: segmentation and airway morphology analysis from low-dose CT scans. Med Imag IEEE Trans 2005;24:1529–1539.
51. Tschirren J, McLennan G, Palagyi K, Hoffman EA, Sonka M. Matching and anatomical labeling of human airway tree. Med Imag IEEE Trans 2005;24:1540–1547.
52. Tschumperlin DJ, Shively JD, Swartz MA, Silverman ES, Haley KJ, Raab G, Drazen JM. Bronchial epithelial compression regulates MAP kinase signaling and HB-EGF-like growth factor expression. Am J Physiol Lung Cell Mol Physiol 2002;282:L904–911. [PubMed: 11943653]
53. Tschumperlin DJ, Shively JD, Kikuchi T, Drazen JM. Mechanical stress triggers selective release of fibrotic mediators from bronchial epithelium. Am J Resp Cell Mol Biol 2003;28:142–9.
54. Tsuda A, Henry FS, Butler JP. Chaotic mixing of alveolated duct flow in rhythmically expanding pulmonary acinus. J Appl Physio 1995;79:1055–1063.
55. Uchida S, Aoki H. Unsteady flows in a semi-infinite contracting or expanding pipe. J Fluid Mech 1977;82(2):371–387.
56. Urquiza SA, Blanco PJ, Venere MJ, Feijoo RA. Multidimensional modelling for the carotid artery blood flow. Comput Methods Appl Mech Engrg 2006;195:4002–4017.
57. van Ertbruggen CV, Hirsch C, Paiva M. Anatomically based three-dimensional model of airways to simulate flow and particle transport using computational fluid dynamics. J Appl Physio 2005;98:970–980.
58. West JB, Matthews FL. Stress, strain, and surface pressure in the lung caused by its weight. J Appl Physio 1972;32:332–345.
59. West, JB. Respiratory physiology. 5. 1995.
60. Xia GH, Zhao Y, Yeo JH, Lv X. A 3D implicit unstructured-grid finite volume method for structural dynamics. Comput Mech 2007;40:299–312.
61. Xia GH, Lin CL. An unstructured finite volume approach for structural dynamics in response to fluid motions. Comput Struct 2008;86:684–701. [PubMed: 18496602]
62. Ye T, Bull JL. Microbubble expansion in a flexible tube. ASME J Biomech Eng 2006;128(4):554–563.
63. Yin Y, Hoffman EA, Lin CL. Mass preserving nonrigid registration of CT lung images using cubic B-spline. Medical Physics 2009;36(9):4213–4222. [PubMed: 19810495]

APPENDIX: SOLVER VALIDATION

Different error analyses and several benchmark cases for verification and validation have been performed on the FSI solver[61]. Here the 3D FSI solver is further validated by performing simulations on a closely-related problem of the flow in a collapsible tube, which has significance in many physiological systems such as blood flow in the circulation and airflow in the airway tree. Given its importance and complexity, the topic of flow through collapsible tubes has been extensively investigated for over 30 years. Kamm and Pedley[18] provided a brief review of the subject, Heil and Jensen[16] gave a more comprehensive review

of the biological examples and the theoretical and computational developments, and Bertram[4] reviewed the experimental side of the subject, and applications in medicine and engineering technologies. Figure A1(A) shows the typical setup of the problem: a flexible tube section of length l is mounted between two rigid tubes of lengths l_{up} and l_{down}, respectively. An external pressure p_{ext} is imposed on the outside wall of the flexible tube section. The pressure at the exit of the downstream rigid tube l_{down} is set to be constant, i.e. $p_{down} = 0$. The radius R of the tube is 4 cm and the thickness h is $R/20$. The length l of the flexible tube is $10R$, and the lengths of the upstream and downstream rigid tubes are R and $5R$ respectively. For the sake of comparison, all the parameters for this case are taken from those used in Marzo *et al.*'s work[31]. The Young's modulus E of the elastic tube is 4,559.4 Pa and the Poisson's ratio is 0.49. A constant flow is imposed at the inlet of the upstream rigid tube, and the Reynolds number is set to be 128. The meshes for fluid and structure domains have 25,578 tetrahedral elements and 3,996 shell triangle-elements, respectively.

The deformation of the flexible section of the tube is determined by the transmural pressure between the internal pressure and external pressure. Initially $p_{ext} = 0$, the internal pressure is larger than $p_{ext,}$ thus the flexible tube expands axisymmetrically under the positive transmural pressure. By increasing the external pressure, the transmural pressure decreases. Eventually the external pressure becomes larger than the internal pressure, and the flexible tube contracts under the negative transmural pressure. If the external pressure exceeds a critical value, the axisymmetric deformation loses its stability and the tube buckles non-axisymmetrically[16]. Figure A1(B) exhibits one example of the non-axisymmetric collapse of the flexible tube. The extent and location of the strongest collapse vary with different external pressure values. Figure A1(C) shows the profiles of the deformed flexible tubes under different external pressures at $p_{ext} = 0.0$ Pa and $p_{ext} = 1.42$ Pa. It is found that at $Re=128$, and with an external pressure $p_{ext} = 1.42$ Pa, the maximum deformation is about $0.8R$, and the location of the maximum collapse point is at 0.76l. Figures A1(D) and A1(E) compare the fluid pressure and wall deformation profiles along the flexible section of the tube with Marzo *et al.*'s result[31], in which the pressure is non-dimensionalized by bending stiffness and the deformation and axial distance are normalized with respect to radius R. Good agreement is found with the results obtained by Marzo *et al.*[31]. Given the non-axisymmetric deformation of the tube, this example suggests that the FSI, which does not assume geometric similarity in expanding or contracting the airways, is a more suitable approach for realistic representation of airway deformation.

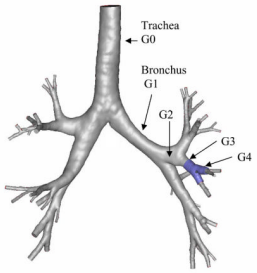

Figure 1.
CT-based human airway model (Ref. [28]).

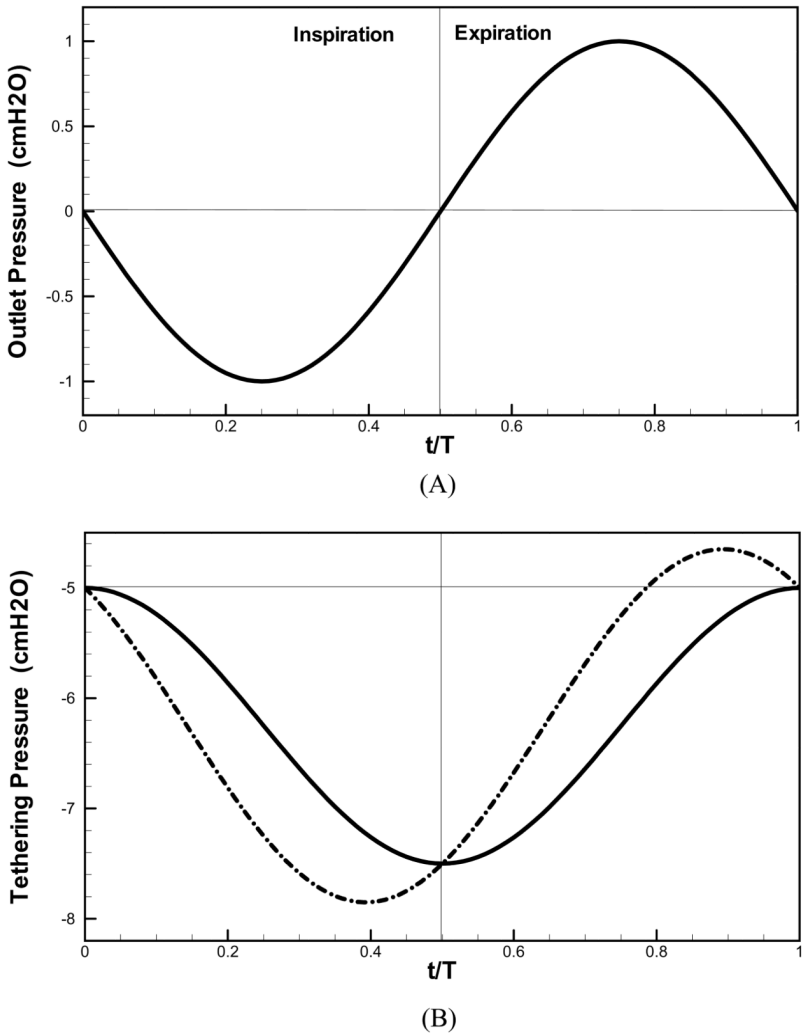

Figure 2.
(A) Outlet pressure, (B) parenchymal tethering pressure (solid line) and resulting pressure (dot-dashed line) profiles for normal breathing (Ref. [59]).

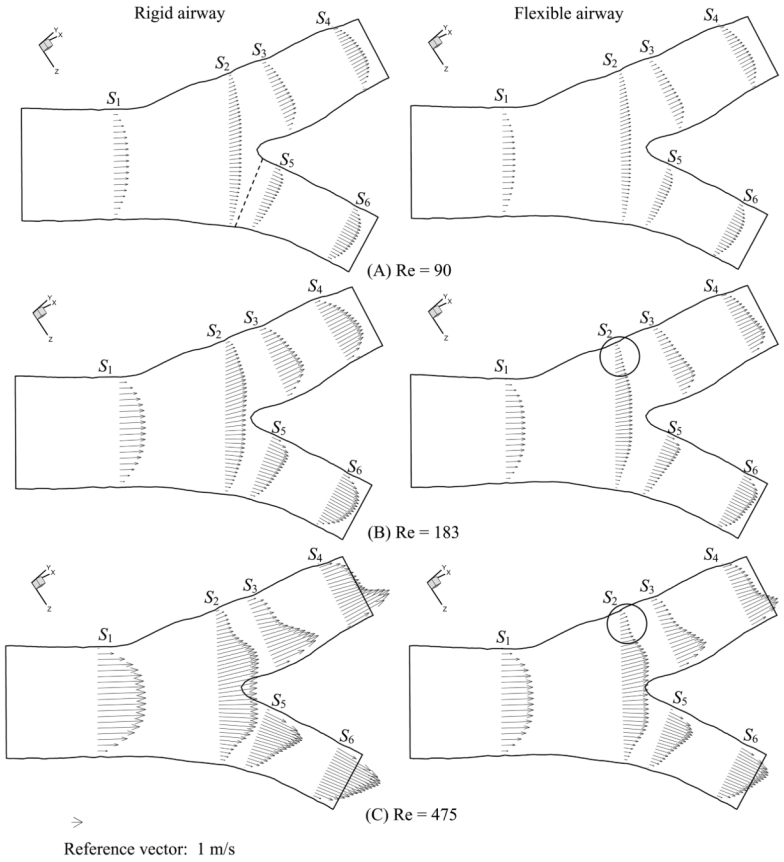

Figure 3.
Velocity profiles at t=0.25T in rigid airway (left panel) and flexible airway (right panel). Re=: (A) 90, (B) 183, and (C) 475.

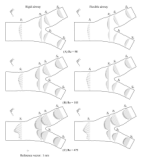

Figure 4.
Velocity profiles at t=0.75T in rigid airway (left panel) and flexible airway (right panel). Re=: (A) 90, (B) 183, and (C) 475.

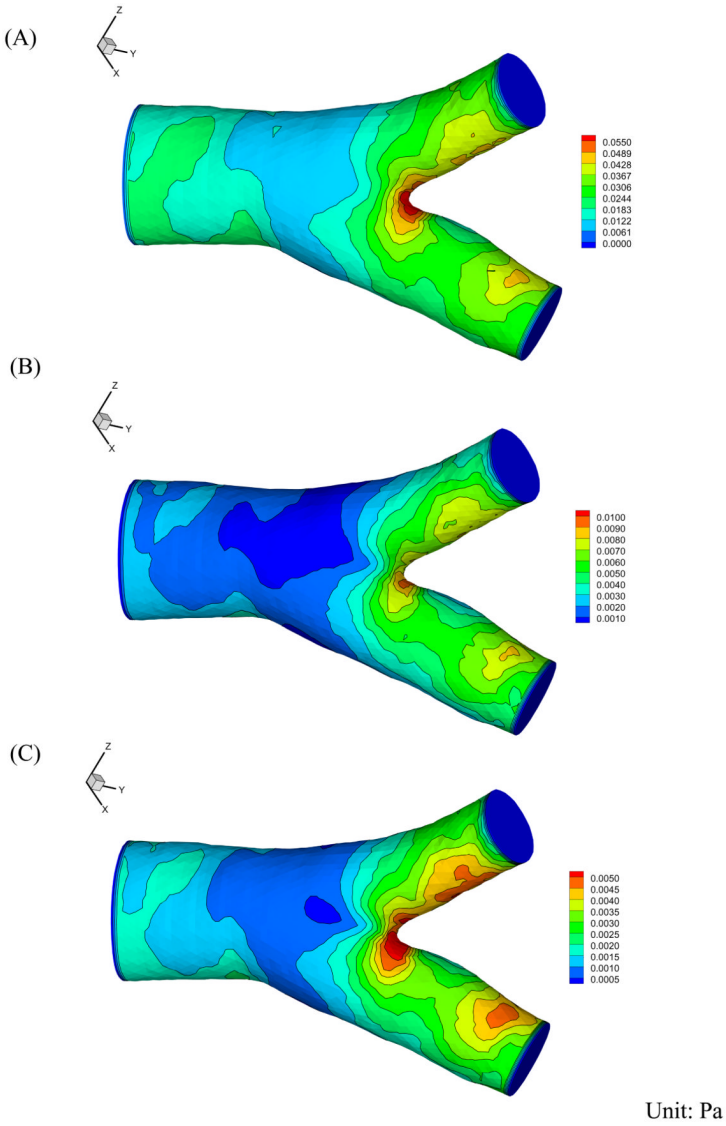

Figure 5.
Wall shear stress distribution at t=0.25T, Re=183 in (A) rigid airway; (B) flexible airway; (C) flexible airway wall with parenchymal tethering.

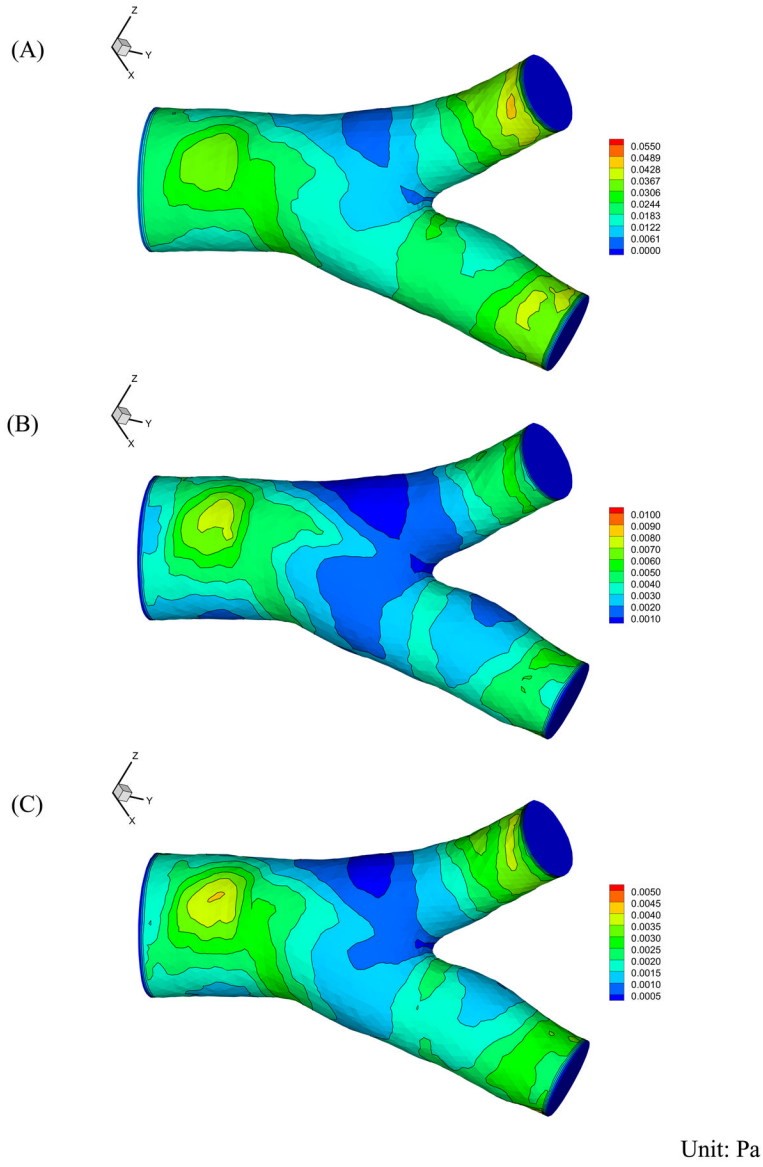

Figure 6.
Wall shear stress distribution at t=0.75T, Re=183 in (A) rigid airway; (B) flexible airway; (C) flexible airway wall with parenchymal tethering.

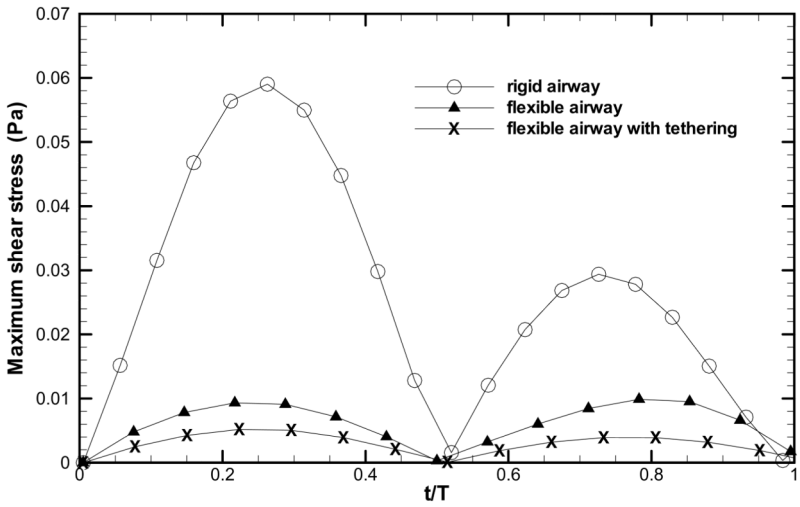

Figure 7.
Time histories of the maximum shear stresses in (A) rigid airway; (B) flexible airway; (C) flexible airway wall with parenchymal tethering.

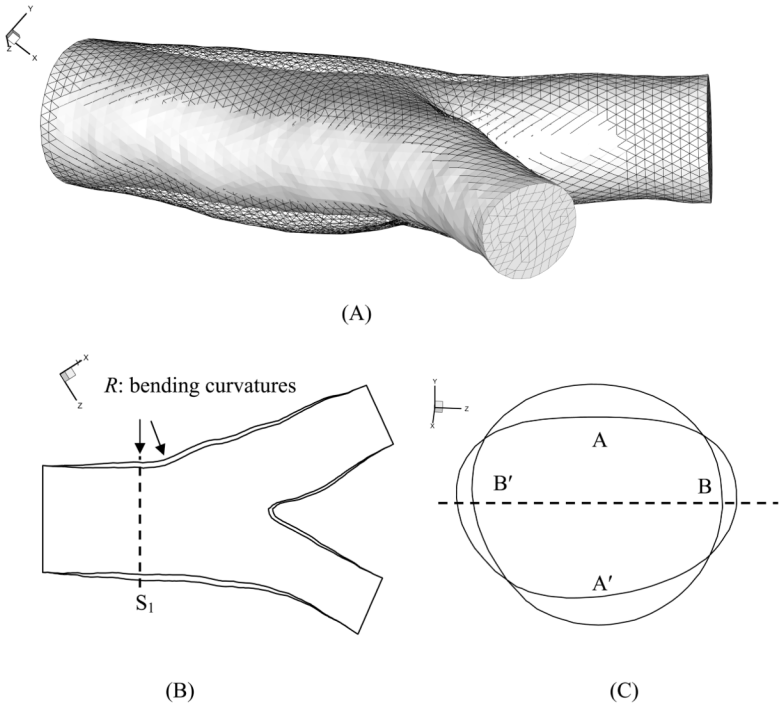

Figure 8.
(A) Volume difference of the airway between the inspiration (black wireframe) and the resting state (shaded) at *Re*=183; (B) deformation in the bifurcation plane, the bending curvature increases as the wall moves from outer line to the inner line; (C) deformation in the transverse plane at station *S*1 (the circular outline, the maximum deformation; the elliptical outline, the resting state; the dashed line, the bifurcation plane).

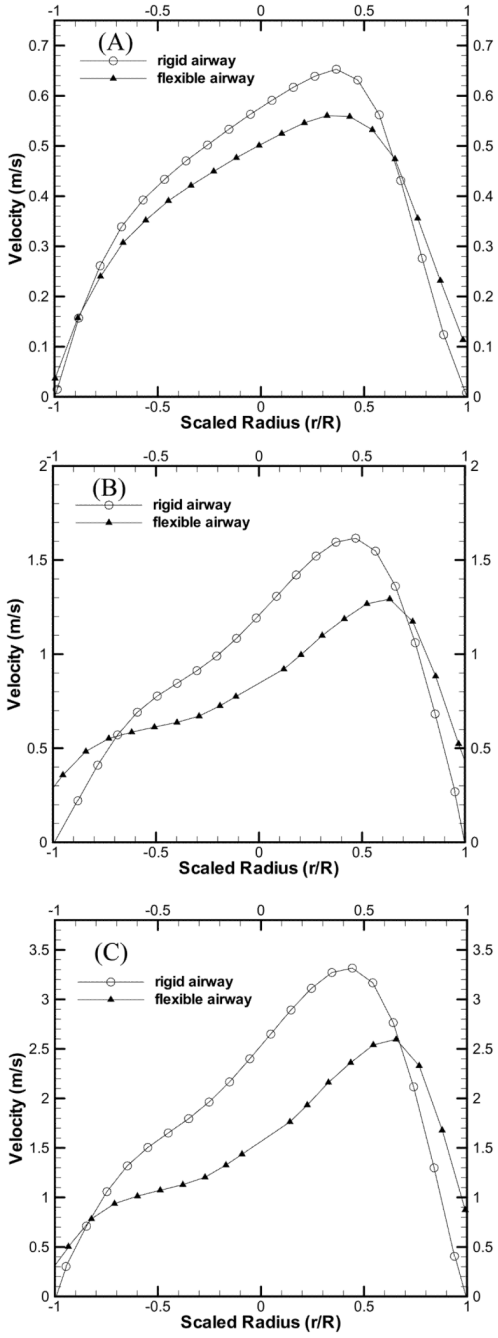

Figure 9.

Comparison of velocity profiles at peak inspiration along the dash line in Figure 3(A) where the maximum shear stress occurs in both rigid and flexible airways for *Re*=: (A) 90, (B) 183, and (C) 475. (The profiles were taken at peak inspiration, when the airway wall velocity is nonzero in the flexible airway model.)

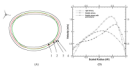

Figure 10.
Comparison of deformations of airway models at peak inspiration with and without lung parenchyma at *Re*=183. (A) Outlines at station *S2* of the inner airway wall at maximum deformation: (1) resting status; (2) *E*=1.0 kPa without lung parenchyma; (3) *E*=2.0 kPa with lung parenchyma; (4) *E*=1.0 kPa with lung parenchyma. (B) Velocity profiles along the dash line in Figure 3(A).

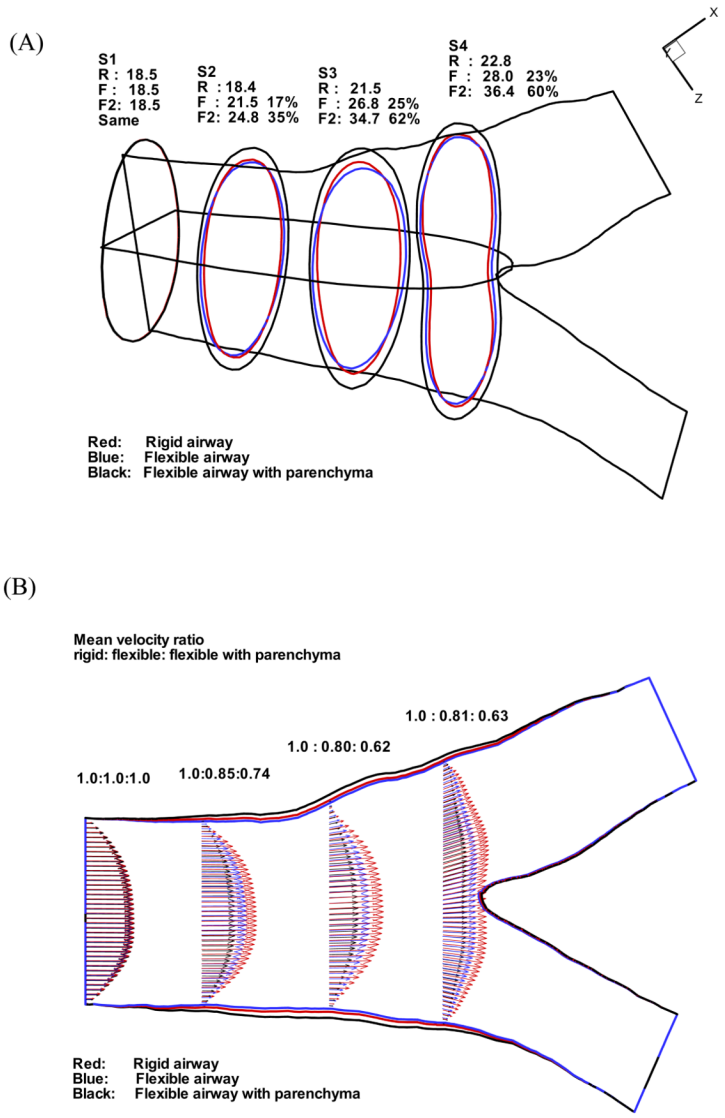

Figure 11.

(A) Comparison of cross-sectional areas at stations S1–S4 at peak inspiration with for the cases of: R, rigid airway; F, flexible airway; F2, flexible airway with tethering. The numbers are the areas (mm^2) and the percentage area changes with respect to the rigid case at that location. (B) Comparison of velocity profiles and mean velocity ratios.

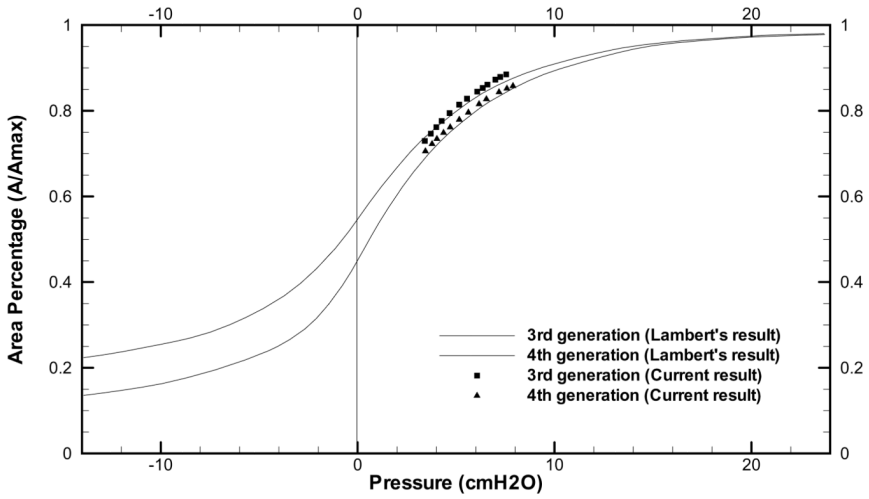

Figure 12.
The relationship between transmural pressure difference and cross-sectional areas, and comparison with Lambert *et al.*'s results (Ref. [26]).

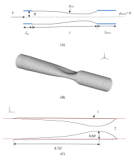

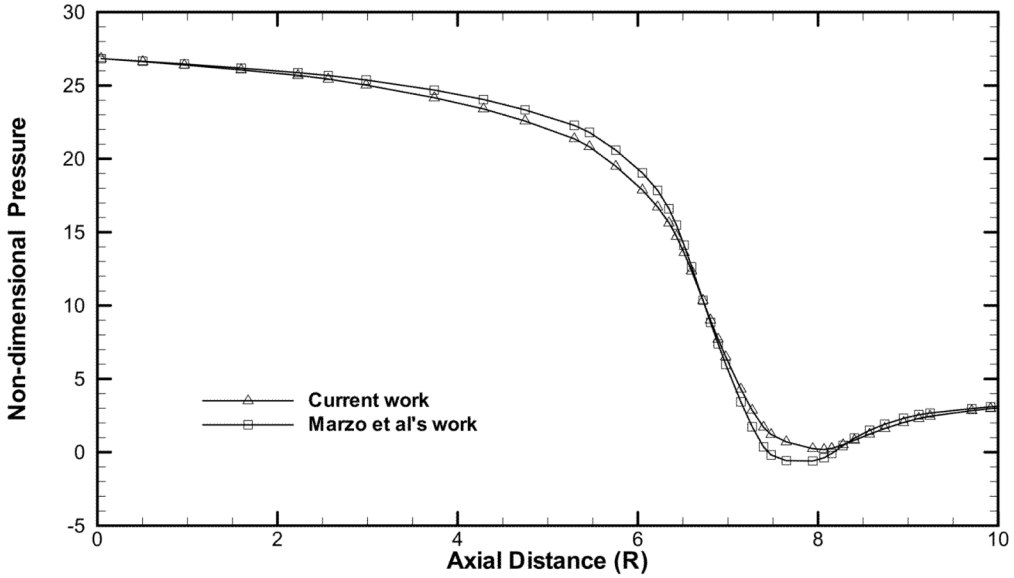

(D)

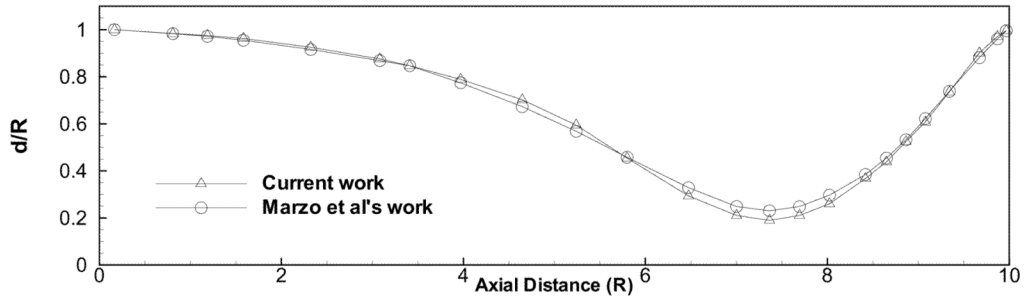

(E)

Figure A1.

(A) Schematic of flow though a collapsible tube. (B) Deformed collapsible tube at p_{ext} =1.4 Pa and *Re*=128, with a maximum deformation of about 0.8*R* at the location 0.72*l* with respect to the beginning point of the flexible section. (C) Profiles of the deformed tube at plane *y*=0 under different external pressures: 1. p_{ext} = 0.0 Pa; 2. *pext* = 1.42 Pa (the dash line is the un-deformed profile). (D) Non-dimensional pressure profiles along the flexible tube section. (E) Deformation profiles of the flexible tube section extracted at *y*-symmetry (*y*=0).

Table 1

Geometric parameters of the airway section (Measured on the CT images taken in Ref. [28]).

Generation	Average Diameter	Average Cross- Sectional Area	Average Wall Thickness
3rd (upper branch 1)	4.85	35.32	2.34
4th (lower branch 2)	3.36	11.67	1.24
4th (lower branch 3)	2.44	5.96	1.20

Unit: mm

Table 2

Geometric parameters of the airway segment. Note that the definitions of the “FRC” and “TLC” for a breathing cycle are given in the text.

Generation	Average Minor Diameter (mm)		Average Cross- Section Area (mm^2)		Volume (mm^3)	
	“FRC”	“TLC”	“FRC”	“TLC”	“FRC”	“TLC”
3rd (upper branch 1)	3.48	4.36	37.40	51.22	624.68	1,147.83
4th (lower branch 2)	2.78	3.16	9.68	12.29	113.13	189.28
4th (lower branch 3)	2.14	2.57	4.94	6.25	62.34	105.78

Table 3

Percentage changes of the airway geometrical parameters and comparison with *in-vivo* CT measurements.

	Average Minor Diameter		Average Cross-Section Area		Volume	
Generation	**Current**	**Saba[45]**	**Current**	**Saba[45]**	**Current**	**Saba[45]**
3rd (upper branch 1)	20.2%	21.0%±1.0%	43.5%	45.20%±2.0%	76.5%	78.50%±5.0%
4th (lower branch 2)	17.3%	18.0%±1.0%	37.6%	38.6%±2.0%	73.2%	76.8%±5.0%
4th (lower branch 3)	17.8%		36.5%		72.5%	